

## Cosmic-ray Isotope Measurements with HELIX

---

**S. P. Wakely,<sup>a</sup> P. S. Allison,<sup>b</sup> M. Baiocchi,<sup>c</sup> J. J. Beatty,<sup>b</sup> L. Beaufore,<sup>a</sup>  
D. H. Calderón,<sup>b</sup> A. G. Castano,<sup>a</sup> Y. Chen,<sup>d</sup> S. Coutu,<sup>d</sup> N. Green,<sup>e</sup> D. Hanna,<sup>f</sup>  
H. B. Jeon,<sup>a</sup> S. B. Klein,<sup>g</sup> B. Kunkler,<sup>g</sup> M. Lang,<sup>g</sup> R. Mbarek,<sup>a</sup> K. McBride,<sup>b</sup>  
S. I. Mognet,<sup>d</sup> J. Musser,<sup>g</sup> S. Nutter,<sup>h</sup> S. O'Brien,<sup>f</sup> N. Park,<sup>c</sup> K. M. Powledge,<sup>a</sup>  
K. Sakai,<sup>a</sup> M. Tabata,<sup>i</sup> G. Tarlé,<sup>e</sup> J. M. Tuttle,<sup>a</sup> G. Visser<sup>g</sup> and M. Yu<sup>d</sup>**

<sup>a</sup>University of Chicago, Enrico Fermi Institute, Chicago, USA

<sup>b</sup>The Ohio State University, Dept. of Physics, Columbus, USA

<sup>c</sup>Queen's University, Dept. of Physics, Engineering Physics and Astronomy, Kingston, Canada

<sup>d</sup>Pennsylvania State University, Dept. of Physics, University Park, USA

<sup>e</sup>University of Michigan, Dept. of Physics, Ann Arbor, USA

<sup>f</sup>McGill University, Dept. of Physics, Montreal, Canada

<sup>g</sup>Indiana University, Dept. of Physics, Bloomington, USA

<sup>h</sup>Northern Kentucky University, Dept. of Physics, Geology and Engineering Technology,  
Highland Heights, USA

<sup>i</sup>Chiba University, Dept. of Physics, Chiba, Japan

E-mail: [wakely@uchicago.edu](mailto:wakely@uchicago.edu)

HELIX (High Energy Light Isotope eXperiment) is a balloon-borne experiment designed to measure the chemical and isotopic abundances of light cosmic-ray nuclei. Detailed measurements by HELIX, especially of  $^{10}\text{Be}$  from  $\sim 0.2$  GeV/n to beyond  $\sim 3$  GeV/n, will provide an essential set of data for the study of propagation processes of the cosmic rays. HELIX consists of a 1 Tesla superconducting magnet with a high-resolution gas tracking system, time-of-flight detector, and a ring-imaging Cherenkov detector. The instrument's first long-duration balloon flight is anticipated to occur in 2024. In this paper, we will briefly discuss the scientific goals of the instrument and report on its design and current status.

38th International Cosmic Ray Conference (ICRC2023)  
26 July - 3 August, 2023  
Nagoya, Japan



## 1. Introduction

Recent precision measurements by a number of space-based instruments have revealed several unanticipated features in the cosmic-ray flux [1, 2]. One of the most striking and well publicized results is the detection of an excess of positrons above 25 GeV, significantly higher than expected from traditional simple propagation models [3, 4]. Various modifications or additions to these models have been proposed to explain this new feature, including the existence of astrophysical positron sources (e.g., [5]), secondary particle production near source regions (e.g., [6]), and dark matter annihilation (e.g., [7]).

In addition, there is now clear evidence of significant deviations, in primary nuclei (e.g., protons and helium) as well secondary nuclei (e.g., lithium and boron), from the simple power-law energy spectra commonly considered in the past [2]. These features certainly indicate that the acceleration and/or propagation processes for cosmic rays are more complex than previously assumed. To aid in furthering our understanding of these puzzles, new data are required, particularly those data that illuminate the features of cosmic-ray secondary production and propagation.

The High Energy Light Isotope eXperiment (HELIX) is a planned series of long-duration balloon payloads proposed to measure light isotopes from  $\sim 0.2$  GeV/n eventually up to  $\sim 10$  GeV/n. The first phase of HELIX is designed to measure isotopes from hydrogen ( $Z = 1$ ) up to neon ( $Z = 10$ ) in the energy range from  $\sim 0.2$  GeV/n up to  $\sim 3$  GeV/n with the detector configuration optimized to measure the ratio of radioactive  $^{10}\text{Be}$  to stable  $^9\text{Be}$ . HELIX is on course to have its first long-duration balloon (LDB) flight from the Esrange space center in Sweden during NASA's spring 2024 LDB campaign.

## 2. Instrument Design

The HELIX instrument, shown in the left panel of Figure 1, is a magnet spectrometer designed to measure light isotopes from protons up to neon ( $Z = 10$ ). Its first iteration, described here, is optimized to achieve an *event-by-event* mass resolution,  $\Delta M/M$ , better than 3%, up to  $\sim 3$  GeV/n. To achieve this, HELIX is designed to provide rigidity and velocity measurements with uncertainties,  $\Delta R/R$  and  $\gamma^2 \Delta \beta/\beta$ , of under 2% over the energy range of interest.

The rigidity measurements are obtained by measuring the trajectories of incident charged particles in a gas drift chamber deployed within a near-uniform 1 T magnetic field. Time-of-flight (TOF) measurements of the particles provide sufficiently accurate velocities up to energies of  $\sim 1$  GeV/n, beyond which a Ring-Imaging Cherenkov (RICH) detector with aerogel radiator is employed. The expected measurements of the  $^{10}\text{Be}/^9\text{Be}$  ratio from the HELIX program (phases 1 and 2) are shown in the right panel of Figure 1, along with existing measurements. Below we discuss some details of the subsystems that comprise the HELIX instrument.

### 2.1 Time-of-Flight and Charge System

The HELIX Time-of-Flight (TOF) and charge system is designed to provide a timing resolution better than 50 ps for nuclei heavier than lithium ( $Z = 3$ ), which is sufficient to measure the velocity of these particles up to  $\sim 1$  GeV/n with the necessary precision. It also measures the charge of incident particles with good linearity up to  $Z = 11$  with resolution better than 0.1 charge units.

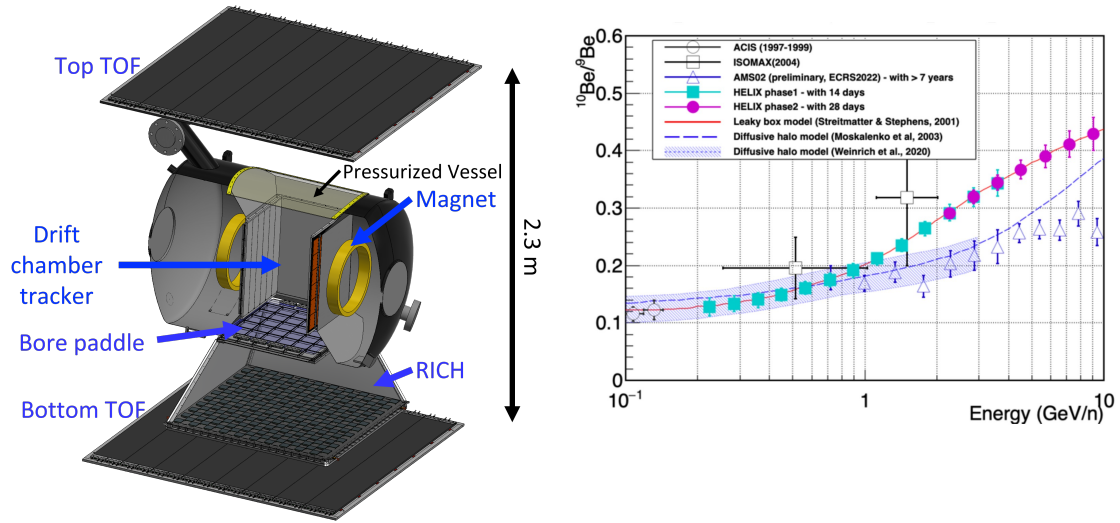


**Figure 1:** Left: Drawing of the HELIX instrument, with key sub-components labeled. Right: Projected  $^{10}\text{Be}/^9\text{Be}$  measurements from HELIX for two phases of the instrument, over multiple flights.

The TOF system consists of two layers of 1.0 cm-thick fast plastic scintillator paddles, located at the top and bottom of the instrumentation stack, with a total separation of 2.3 m (see Figure 1). Each layer consists of 8 paddles of Eljen Technologies EJ-200 custom-cast plastic scintillator, each with dimensions of  $20 \times 160 \text{ cm}^2$ . The upper TOF assembly is shown in the left panel of Figure 2. The paddles are wrapped in highly reflective Teflon and then overwrapped with light-tight Tedlar material. An additional EJ-200 scintillator slab ( $1.0 \times 60.6 \times 60.6 \text{ cm}^3$ ) is located just beneath the magnet bore and is used to define the instrument trigger (along with the top/bottom TOF planes), as well as to provide additional charge and timing information.

Readout of the scintillators is accomplished with Hamamatsu S13360-6050VE silicon photo-multipliers (SiPMs). Each top/bottom scintillator paddle is coupled to two carrier boards on each end, each with 4 SiPMs (16 total per paddle). The bore paddle is read out using 4 carrier boards (16 SiPMs) along each of two opposite ends. The SiPMs feature large dynamic range and high photo-detection efficiency, a fast (0.9 ns) risetime, and low transit-time skew. They are read out using custom electronics and are digitized for timing and charge information. Each SiPM's operational bias voltage is independently controllable to achieve uniform gain. As the temperature/gain coefficient is similar for all SiPMs, the bias voltage is automatically adjusted for gain stabilization based on a common temperature sensor located on each carrier board of 4 SiPMs.

Signals from the SiPM carrier boards are routed in groups of 8 to a readout board. A DC-coupled fast output is connected to a leading-edge discriminator, the output of which is connected to a time-to-amplitude converter sampled by a 14-bit ADC running at 40 MSPS. This time-to-digital converter (TDC) configuration has a timing resolution better than 25 ps. A slow output from the SiPM carrier board is shaped and then sampled with another 40 MSPS ADC channel. This output is also used to provide an overall instrument trigger with two discriminator thresholds, allowing for independent low-charge and high-charge triggers, with optional pre-scaling on either. The data from the 16 channels of ADC on the readout board are received and packaged for transmission to

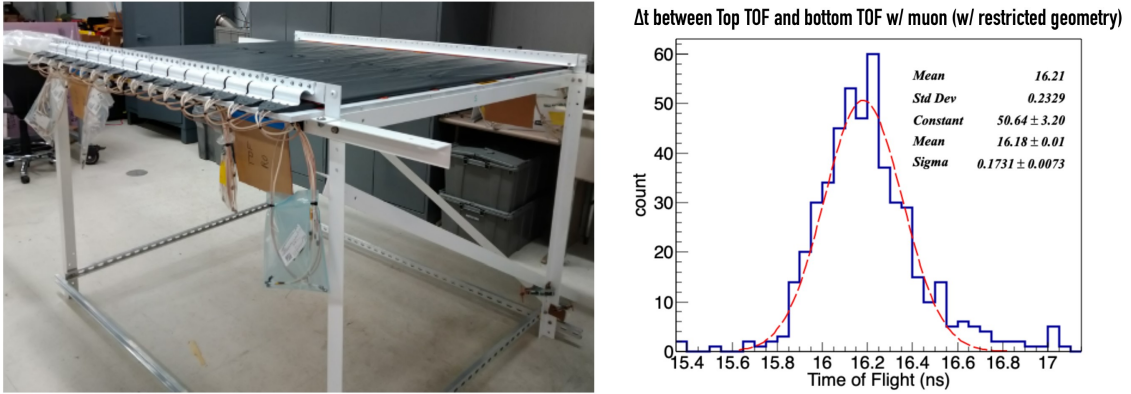


**Figure 2:** Left: Top TOF layer on the HELIX upper gondola frame. Right: Time difference between hits in the upper and lower scintillator paddles, as measured by the flight readout system, for a ground-level muon run.

the HELIX DAQ by a Xilinx Artix-7 FPGA, which also handles slow controls of the readout board including the SiPM bias system.

## 2.2 Spectrometer

### 2.2.1 Magnet

The HELIX magnet consists of two Nb-Ti superconducting coils contained within a 260L liquid helium cryostat that can provide a hold time of  $\sim 7$  days at float altitudes. Initially designed and built for the HEAT experiment [8], the magnet has been used in five previous balloon campaigns, where it was operated at 1 atmosphere, maintained by an external pressure vessel. For HELIX, the magnet and all control and housekeeping systems, including the magnet discharge system, have been reconfigured for low-pressure operations without an external vessel. An automated 3D scan of the magnetic field in the bore volume has verified that the magnet continues to perform as designed, with close agreement to its original analytic field model. In addition, the magnet has been successfully tested in vacuum chambers twice since the reconfiguration and has undergone multiple full-field tests in the lab.

### 2.2.2 Drift-Chamber Tracker

The HELIX Drift-Chamber Tracker (DCT), which measures the rigidity and trajectory of through-going charged particles, is located within the bore of the magnet (see Figure 3). The detector has an active volume of  $45 \times 45 \times 58 \text{ cm}^3$ , and is installed within a sealed vessel that maintains a gas pressure of 1 atmosphere during flight. A mixture of 90%  $\text{CO}_2$  and 10% argon provides low thermal diffusion and good operating stability. The interior geometry of the DCT consists of 3 sense-wire planes and 4 cathode planes. The interior cathode planes consist of  $250\text{-}\mu\text{m}$ -diameter gold-plated aluminum wires, while the outer cathode planes are formed by gold-plated printed circuit boards. Each sense-wire plane consists of 72  $20\mu\text{m}$ -diameter resistive sense wires interspersed with  $250\mu\text{m}$  potential wires operating at a nominal voltage of  $-3 \text{ kV}$ . The nominal cathode voltage is  $-10 \text{ kV}$ . The drift region between each cathode and sense-wire plane is completely surrounded by field-shaping electrodes consisting of a set of 4 mm pitch field-shaping strips, providing a uniform drift field of

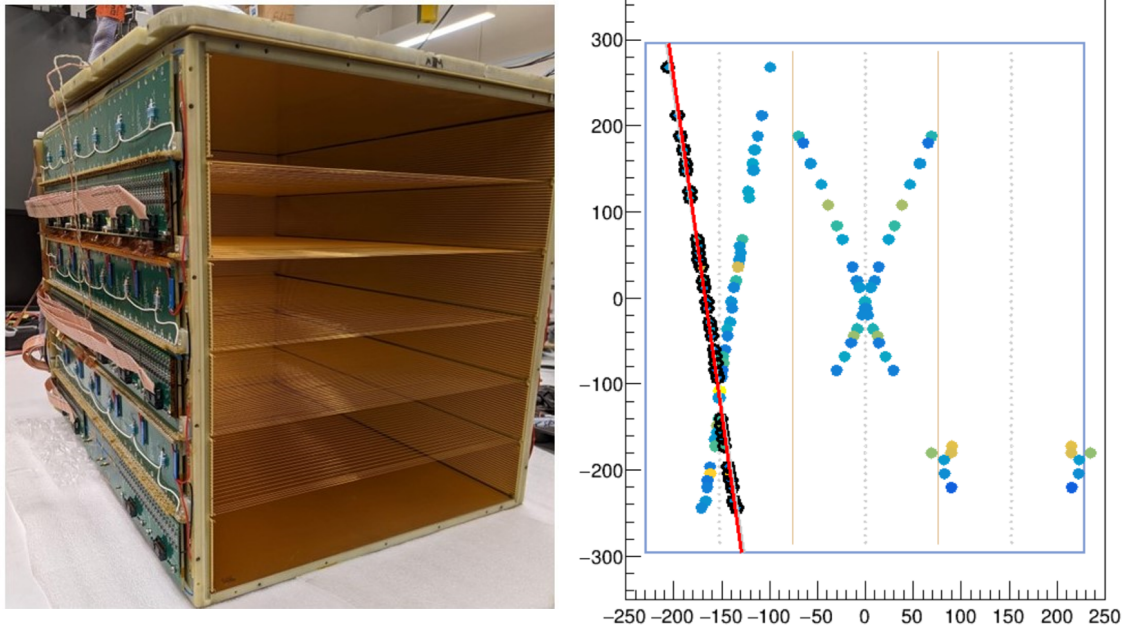


**Figure 3:** Left: A picture of the DCT on its side with its top open, showing 3 drift cells per layer with 2 drift-field wires on either side of the central drift cell. The sense wires are difficult to see and the gold wires that are visible are the drift-field and field-shaping wires, which have a larger diameter. The FEEs for one side of the sense wires are visible on the outside of the left face. Right: An image from the online event display showing a pair of particle tracks in the bending plane of the DCT, with color scale representing the quantity of charge in each hit. The mirrored hits about the sense wires demonstrate the left-right ambiguity inherent in drift chambers. The darker hits are those selected by the image analysis software as the most likely true track among the left-most set of mirrored hits.

1.3 kV/cm in the drift volume. Alternate sense wires are staggered in the drift plane by 0.3 mm to aid in resolving left-right ambiguity (see more in [9]).

The sense wires have a nominal resistance of 1.8 k $\Omega$ , which is used to provide charge-division-based tracking in the non-bending plane, while drift-time measurements provide high-resolution tracking in the bending plane. Each sense wire end is terminated at a chamber-mounted front-end (FE) board assembly. Sense wire signals are amplified by this assembly and sent to ADC boards located outside of the pressure vessel via custom hermetic bulkhead feedthroughs. Each FE board handles signals from 24 sense wires. Each ADC board processes signals from 48 wire ends, and provides full waveform digitization of the 10  $\mu$ s drift window following an event trigger. The sample rate is 80 MSPS at 12 bit resolution. The ADC board supports hardware zero-suppression of portions of the waveform falling below a programmable signal threshold, restricting readout to regions of interest that have crossed threshold. All relevant readout parameters can be adjusted during flight if needed.

More details on the DCT can be found in these proceedings [9].

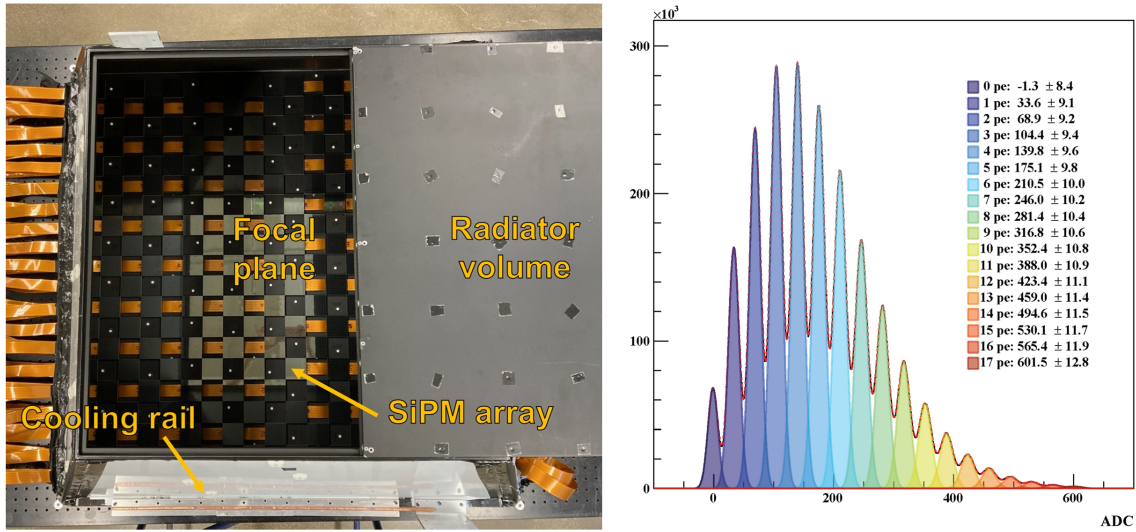


**Figure 4:** Left: A photo of the top view of the RICH, with parts labeled. 200 SiPM arrays are populated on the focal plane in a checkerboard pattern, with orange cables routed out the side. Right: A charge histogram for 12,697 gain-matched SiPM channels on the RICH focal plane, in response to laser calibration flashes. 0.8% of the channels are omitted due to noise or various malfunctions. A clear peak separation with spacing of  $\sim 36$  ADC per photoelectron is shown up to 17 photoelectrons.

### 2.3 Ring-Imaging Cherenkov Detector and Hodoscope

The HELIX RICH detector (Figure 4) is designed to measure the velocity and charge of nuclei with energies greater than  $\sim 1$  GeV/n. Located under the bore paddle, the proximity-focused RICH consists of a 1 cm-thick radiator and a  $1 \text{ m}^2$  focal plane separated by an expansion length of 50 cm. The radiator consists of a  $6 \times 6$  array of tiles, each of which is  $10 \times 10 \text{ cm}^2$ . The majority of the tiles consist of transparent, hydrophobic aerogel with a high refractive index (RI) of  $\sim 1.15$ , fabricated at Chiba University using a novel pinhole-drying technique [10]. Because there is some RI variation from tile to tile and within each tile, each one must be calibrated and mapped to the level of  $\sim 10^{-4}$  to achieve the precision requirements of the RICH. This mapping has been successfully performed using a number of techniques, including electron beam tests [11]. In addition to the aerogel, four high-index ( $n=1.33$ ) sodium fluoride blocks are installed in the array to provide a lower energy threshold, allowing cross-calibration between the TOF and the RICH.

The RICH focal plane is instrumented with 200 Hamamatsu S14498 SiPM arrays, arranged in a checkerboard pattern. These arrays were designed by Hamamatsu for the HELIX experiment and feature 64 individual  $6 \times 6 \text{ mm}^2$  pixels with  $75 \mu\text{m}$  microcells and  $\sim 55\%$  photon detection efficiency at 450 nm, and integrated array-level temperature sensors. To reduce the material in the instrument acceptance, the SiPM arrays are read by 70 cm-long flexible circuit-board cables connecting to front-end electronics boards mounted at the sides of the gondola. To reduce dark rates, the focal plane is temperature-controlled using thermoelectric coolers coupled to a coolant loop and a passive radiator system. The focal plane and Cherenkov radiators are enclosed in a lightweight aluminum dark-box structure.

The readout of RICH signals is achieved using 32-channel CITIROC 1A [12] ASICs from

WEEROC. Each RICH front-end board contains 16 chips, and hence can read out 8 SiPM arrays, for 512 channels per board, and 12,800 channels for the entire system. The output of each SiPM pixel is amplified and split into fast-trigger and charge-output paths. The trigger path is used to collect timing information on photon hits with a resolution better than 12.5 ns, which can be used to suppress dark-count backgrounds. The charge path feeds a slow shaper and a sample-and-hold circuit to provide multiplexed pulse-height outputs to an off-chip 12-bit ADC for readout. The bias voltage of each SiPM channel in the RICH can be individually trimmed within the CITIROC to provide uniform gain across the focal plane. The RICH board provides a trigger threshold as low as 0.3 photoelectrons (PEs) and is designed to provide a linear dynamic range up to  $\sim 100$  PEs.

For gain calibrations, a 405nm pulsed laser system is employed in calibration runs to illuminate the focal plane through fiber-optic cannulae mounted on the walls of the RICH. The result of such a process is demonstrated in the right panel of Figure 4, which shows excellent calibration of more than 99% of the RICH pixels to a fixed ADC/PE gain level.

### 2.3.1 Hodoscope

To reduce tracking uncertainty in the non-bending plane of the spectrometer, a scintillating fiber hodoscope has been introduced directly above the RICH radiator volume. The hodoscope consists of four 150-fiber ribbons arranged in a single layer. Each ribbon is made of BCF12 plastic scintillating fibers from Saint-Gobain Crystals; each fiber has a 1 mm  $\times$  1mm square cross section and a length of 1 m. The active hodoscope area is 60 cm  $\times$  60 cm, covering the full bore.

The hodoscope is read out using the same SiPM arrays and electronics as the RICH. Hence, the fibers at the end of each ribbon are woven into a Delrin cookie with a position-multiplexed pattern wherein two or three fibers are assigned to a single SiPM pixel within the array. The tracking accuracy of the DCT is sufficient to select between multiplex units within the hodoscope channel map, allowing the correct fiber to be assigned to the hit, ultimately providing a sub-millimeter hit location.

More details on the RICH and hodoscope can be found in these proceedings [13].

## 3. Status and Future Plans

In mid-2021, a one-week cool-down test of the HELIX magnet was performed, during which all front-end electronics and power components, including key NASA support components, were successfully tested at their flight magnetic field. This was followed, in early 2022, by a full-instrument thermal vacuum test at the B-2 chamber of the Armstrong Test Facility in Sandusky Ohio. The payload spent 24 hours at float pressures under a number of simulated solar flux conditions, revealing no serious thermal issues.

The HELIX instrument is currently assembled and completing integration in the high-bay balloon facility at the University of Chicago. All major subsystems have been delivered and are undergoing testing with ground-level muons. The first long-duration balloon flight of the payload, which will serve as an engineering checkout of all the subsystems, is scheduled to take place during the Spring 2024 CSBF Kiruna, Sweden campaign.

## Acknowledgements

This work is supported in the US by grant 80NSSC20K1840 from the National Aeronautics and Space Administration (NASA) and in Canada by grants from the Natural Sciences and Engineering Research Council (NSERC) and the Canadian Space Agency's Flights and Fieldwork for the Advancement of Science and Technology (FAST) program.

## References

- [1] Philipp Mertsch. In: *arXiv e-prints*, arXiv:2110.03325 (Oct. 2021). arXiv: [2110.03325](https://arxiv.org/abs/2110.03325) [[astro-ph.HE](#)].
- [2] S Gabici. In: Proc. of the 38th International Cosmic Ray Conference (Nagoya). 2023.
- [3] O. Adriani et al. In: *Nature* 458 (Apr. 2009), pp. 607–609. doi: [10.1038/nature07942](https://doi.org/10.1038/nature07942). arXiv: [0810.4995](https://arxiv.org/abs/0810.4995).
- [4] L. Accardo et al. In: *Phys. Rev. Lett.* 113 (12 2014), p. 121101. doi: [10.1103/PhysRevLett.113.121101](https://doi.org/10.1103/PhysRevLett.113.121101). URL: <https://link.aps.org/doi/10.1103/PhysRevLett.113.121101>.
- [5] Silvia Manconi et al. In: *Phys. Rev. D* 102 (2 2020), p. 023015. doi: [10.1103/PhysRevD.102.023015](https://doi.org/10.1103/PhysRevD.102.023015). URL: <https://link.aps.org/doi/10.1103/PhysRevD.102.023015>.
- [6] Ruizhi Yang and Felix Aharonian. In: *Phys. Rev. D* 100.6, 063020 (Sept. 2019), p. 063020. doi: [10.1103/PhysRevD.100.063020](https://doi.org/10.1103/PhysRevD.100.063020). arXiv: [1812.04364](https://arxiv.org/abs/1812.04364) [[astro-ph.HE](#)].
- [7] Ilias Cholis et al. In: *Journal of Cosmology and Astroparticle Physics* 2009.12 (2009), p. 007. doi: [10.1088/1475-7516/2009/12/007](https://doi.org/10.1088/1475-7516/2009/12/007). URL: <https://dx.doi.org/10.1088/1475-7516/2009/12/007>.
- [8] S. W. Barwick et al. In: *Nuclear Instruments and Methods in Physics Research A* 400 (Feb. 1997), pp. 34–52. doi: [10.1016/S0168-9002\(97\)00945-5](https://doi.org/10.1016/S0168-9002(97)00945-5).
- [9] Keith McBride et al. In: Proc. of the 38th International Cosmic Ray Conference (Nagoya). 2023.
- [10] Makoto Tabata et al. In: *Nuclear Instruments and Methods in Physics Research A* 952, 161879 (Feb. 2020), p. 161879. doi: [10.1016/j.nima.2019.02.006](https://doi.org/10.1016/j.nima.2019.02.006). arXiv: [1901.06663](https://arxiv.org/abs/1901.06663) [[physics.ins-det](#)].
- [11] P. Allison et al. In: *Nuclear Instruments and Methods in Physics Research A* 1055, 168549 (Oct. 2023), p. 168549. doi: [10.1016/j.nima.2023.168549](https://doi.org/10.1016/j.nima.2023.168549). arXiv: [2307.09689](https://arxiv.org/abs/2307.09689) [[astro-ph.IM](#)].
- [12] J Fleury et al. In: *Journal of Instrumentation* 9.01 (2014), pp. C01049–C01049. doi: [10.1088/1748-0221/9/01/c01049](https://doi.org/10.1088/1748-0221/9/01/c01049). URL: <https://doi.org/10.1088/1748-0221/9/01/c01049>.
- [13] Hyebin Jeon et al. In: Proc. of the 38th International Cosmic Ray Conference (Nagoya). 2023.